RSC Advances

PAPER

Cite this: *RSC Adv.*, 2016, **6**, 76542

One-pot solvothermal synthesis of magnetic $SnFe_2O_4$ nanoparticles and their performance in the photocatalytic degradation of chlortetracycline with visible light radiation

Yuefa Jia,[a] Deok-Hyeon Kim,[a] Taehyoung Lee,[b] Seokwon Kang,[b] B. W. Lee,[a] S. J. Rhee[a] and Chunli Liu*[a]

Highly crystalline $SnFe_2O_4$ nanoparticles with high saturation magnetization and superior chlortetracycline (CTC) degradation efficiency was developed using a one-pot solvothermal method. The $SnFe_2O_4$ nanoparticles about 50 nm were prepared with a simple and cost-effective process performed at 200 °C. Superparamagnetism was observed from the $SnFe_2O_4$ nanoparticles with a high saturation magnetization of 74.3 emu g^{-1}. The excellent photocatalytic activity of the $SnFe_2O_4$ nanoparticles was demonstrated through the high degradation efficiency of CTC under a visible light/$SnFe_2O_4$/9 mM H_2O_2 process. The effective degradation of CTC with the $SnFe_2O_4$ nanoparticles was attributed to the effective absorption of the visible light and the good separation ability of the electron–hole pairs. The synergy effect between $SnFe_2O_4$ and H_2O_2 was analysed, and the optimum initial concentration of H_2O_2 was determined to be 9 mM to achieve the best photocatalytic result on CTC. The $SnFe_2O_4$ nanoparticles also exhibited a fast and easy magnetic retrieval and a stable performance with continuous recycled usage.

Received 13th June 2016
Accepted 1st August 2016

DOI: 10.1039/c6ra15312g

www.rsc.org/advances

1. Introduction

Tetracyclines (TCs) are well-known antibacterial compounds for treating disease and protecting the health of both humans and animals. Among the TC family, chlortetracycline (CTC) are widely used in nutrition and feed additives for livestock in many countries,[1] and consequently the residual CTC are detected in the aquatic environment including surface water. Previous studies have reported that CTC were toxic on fresh-water algae and phytoplankton, which indicated the potential of the negative effects of CTC on the ecosystem equilibrium.[2,3] Accordingly, the removal of CTC from wastewater or natural water raised increasing concerns for environmental protection. It is relatively difficult to remove CTC *via* biological/physicochemical treatment processes because of their antibiotic nature, the hydrophilic property, and the stable naphthacene ring structure.[4,5] Hence, various technologies have been investigated for the effective removal of residual CTC, such as the photoelectrocatalytic oxidation processes,[6,7] the advanced oxidation processes[8,9] and photolysis/photooxidation.[10,11] Among the abovementioned techniques, photocatalysis has been considered as the most promising way to remove stable organic pollutant from water through oxidation imparted by the hydroxyl radicals.[12,13] Although quite efficient photocatalytic reactions carried out in suspension have been demonstrated, the difficulty in separation and recycle the photocatalyst materials has been considered as a limitation for the practical application of these photocatalytic processes for water treatment.

Spinel ferrites have the general formula as MFe_2O_4 (M = Fe, Co, Ni, Mn, *etc.*), and the transition metal ions and Fe ions are distributed on the divalent (tetrahedral) and trivalent (octahedral) sites, respectively. Due to their enriched magnetic and electrical properties, spinel ferrites have been studied for various applications including magnetic recording, microwave devices, and biomedical materials.[14] Recently spinel ferrites such as Fe_3O_4,[15,16] $CoFe_2O_4$,[17] $ZnFe_2O_4$,[18] $MnFe_2O_4$,[19] and $NiFe_2O_4$ [20] have been reported for their effectiveness in removing organic pollutants from wastewater. The relatively narrow band gap and superparamagnetic property enabled the spinel ferrite nanomaterials for visible-light assisted photocatalyst application with easy magnetic retrieval. The additional advantage of spinel ferrites is that the Fe ions can react with the adsorbed hydrogen peroxide molecules through Fenton-like redox reactions to produce hydroxyl radicals, which are the most important items in the oxidative removal of organic pollutants under visible light.[21–24] As compared with other popular spinel ferrites, the synthesis of $SnFe_2O_4$ had been difficult to achieve at low temperatures till the recent reports

[a]*Department of Physics and Oxide Research Center, Hankuk University of Foreign Studies, Yongin 449-471, Korea. E-mail: chunliliu@hufs.ac.kr; Tel: +82-31-330-4733*
[b]*Department of Environmental Science, Hankuk University of Foreign Studies, Yongin 449-471, Korea*

using a precipitation exchange approach and similar techniques.[25–27] Since then the inverse spinel $SnFe_2O_4$ nanoparticles have been studied for their synthesis and magnetic properties,[28,29] and more interestingly, $SnFe_2O_4$ has been demonstrated to be quite effective in the photocatalytic degradation of organic pollutants.[30] The abundance of Sn and Fe elements on earth and their non-toxic nature give favorable advantages for $SnFe_2O_4$ as a promising photocatalyst for organic pollutants.[27,31]

It is well-known that the synthesis conditions and processes have great influence on the physical and chemical properties of the spinel ferrite nanostructures. Various methods including precipitation exchange,[25,26] co-precipitation,[27,28,31] high energy ball milling[29] and solvent-assisted interfacial reaction[30] have been reported for the synthesis of $SnFe_2O_4$ nanoparticles, but the crystallinity and magnetization need to be improved in order to achieve desired photocatalytic performance. Furthermore, no study has been yet reported on its photocatalytic degradation of CTC with aqueous H_2O_2 under visible light irradiation. In this work, we report the successful preparation of $SnFe_2O_4$ nanoparticles with good crystallinity and high saturation magnetization *via* a one-pot solvothermal method, and evaluate the photocatalytic activity of $SnFe_2O_4$ nanoparticles using CTC as a target contaminant under visible light irradiation together with H_2O_2. Fast degradation rate of CTC, good recycling property, and easy magnetic retrieval are demonstrated using the high quality $SnFe_2O_4$ nanoparticles prepared in this work.

2. Experiment section

2.1 Synthesis of $SnFe_2O_4$ nanoparticles

$SnFe_2O_4$ nanoparticles were prepared with a one-pot solvothermal (ST) method. First, $SnCl_2$ and $FeCl_2 \cdot 4H_2O$ with a stoichiometric ratio of 1 : 2 were dissolved in 50 mL ethylene glycol under constant stirring to form a solution. Subsequently, a suitable amount of aqueous NaOH and NH_4OH was added to the above solution and the mixture was stirred vigorously at 50 °C for several hours before being transferred to a Teflon-lined stainless steel autoclave with a volume of 100 mL. The autoclave was placed in a furnace held at 200 °C for 16 h, and allowed to cool to room temperature. Finally, the resulting products were washed using ethanol for several times and dried in air at 60 °C for 12 h. The final product was denoted as $SnFe_2O_4$ (ST). For comparison, $SnFe_2O_4$ nanoparticles were also synthesized by precipitation exchange (PE) method as reported by Liu *et al.*[25,26] and were denoted as $SnFe_2O_4$ (PE).

2.2 Characterization methods

The phase structure of the samples was characterized by a Rigaku MiniFlex 600 X-ray diffraction (XRD) using a Cu K_α ($\lambda =$ 0.15418 nm) radiation. The morphology and microstructure of the samples were observed by a field emission scanning electron microscopy (FESEM, Hitachi-S4800) equipped with energy-dispersive X-ray (EDX) and a high resolution transmission electron microscope (HRTEM, JEOL, JEM-3000F). Lakeshore 7403 vibrating sample magnetometer (VSM) was used to measure the magnetic properties of samples. The XPS measurements were performed using a mono-chromated Al K_α X-ray source ($h\nu = 14\ 86.6$ eV) at 15 kV/150 W. The spot size used was 400 mm (Theta Probe AR-XPS System, Thermo Fisher Scientific, Waltham, MA, USA). Fourier transfer infrared spectroscopy (FT-IR), photo-luminescence spectra (PL) and UV-vis diffuse reflectance spectra (UV-vis DRS) were recorded by a Nicolet Avatar 370 FT-IR, RF-5301 fluorescence spectrophotometer and an U3010 UV-vis spectroscopy, respectively. The zeta potential of sample was measured with a Zetasizer 3000HS nanoparticles and potential analyzer.

2.3 Photocatalytic degradation of CTC

The photocatalytic experiments are carried out in the device as described elsewhere.[32] The experimental procedure was as follows: 70 mg of photocatalyst was first dispersed in 70 mL CTC (50 mg L^{-1} in H_2O, $C_{22}H_{23}ClN_2O_8 \cdot HCl$: ≥75%, Sigma-Aldrich Chemicals Co.) in a quartz tube, which was then sonicated for 10 min and stirred at 900 rpm continuously for 1 h before light irradiation to ensure an adsorption–desorption equilibrium. Next, H_2O_2 (30 wt%) was added to the mixture in the quartz tube and the mixture was then irradiated with a 300 W iodine tungsten lamp located 20 cm away from the visible source. All the tests were performed at room temperature. At given time intervals, 5 mL of the suspension was filtered through the 0.2 μm membranes and centrifuged to measure the residual concentration of CTC by a UV-vis spectrophotometer (Cary 5000 UV-vis-NIR, Agilent) at 354 nm. To test the recyclability of the catalyst, the $SnFe_2O_4$ nanoparticles were collected with an external magnet after CTC had been decomposed, then washed and dried at 100 °C for 4 h before being used for the subsequent recycling experiments. The recycling test was repeated for three cycles under the same experimental conditions, and a fresh CTC solution was used in each experiment cycle.

3. Results and discussion

3.1 Crystal and microstructure phase analysis

Fig. 1 shows the XRD diffraction patterns of the $SnFe_2O_4$ nanoparticles synthesized by the ST and the PE method, which matches well with other reports for $SnFe_2O_4$.[25–27,30] The diffraction peaks of $SnFe_2O_4$ at 2θ values of 30.1°, 35.45°, 37.14°, 43.12°, 53.48°, 57.01° and 62.59° was indexed to the (220), (311), (222), (400), (422), (511) and (440) planes, respectively. Furthermore, no extra diffraction peaks can be identified in Fig. 1, implying the presence of only one crystalline product in the sample. It is observed that the intensities of the XRD peaks of $SnFe_2O_4$ (ST) nanoparticles were much stronger than those of $SnFe_2O_4$ (PE), implying a much better crystallinity in $SnFe_2O_4$ (ST). The average crystalline size of $SnFe_2O_4$ (ST) and $SnFe_2O_4$ (PE) nanoparticles calculated from Scherrer equation is 25 nm and 18 nm, respectively.

Fig. 2a and b displays the typical HRSEM micrographs obtained from the $SnFe_2O_4$ (ST) and $SnFe_2O_4$ (PE) nanoparticles. It is easily seen that the $SnFe_2O_4$ (ST) nanoparticles are nearly spherical with a quite uniform size about 50 nm. In addition,

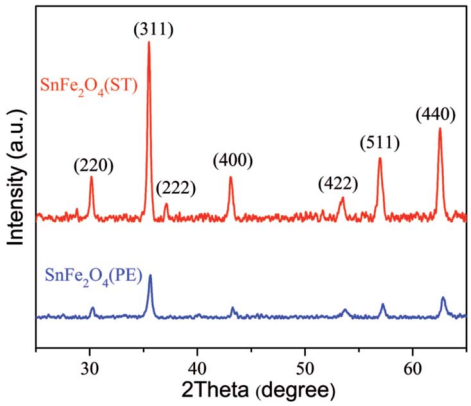

Fig. 1 XRD patterns of $SnFe_2O_4$ nanoparticles synthesized by the ST and the PE methods.

EDX was used to determine the Sn : Fe ratio at points 1 (inset of Fig. 2a). The results revealed that Sn and Fe was 33.56% and 30.36% (weight%) and thus the molar ratio of Sn to Fe is approximate 1 : 2 at point 1, meaning that the spherical-shaped particles are nearly stoichiometric $SnFe_2O_4$. $SnFe_2O_4$ (PE) nanoparticles with an average size of approximate 10–20 nm can be clearly observed from Fig. 2b, which is close to the previous reported results.[25,26] The morphology and element analysis of $SnFe_2O_4$ (ST) nanoparticles were further depicted by TEM in Fig. 2c. Those images also clearly demonstrate that the nanoparticle average size is about 50 nm, in good consistency with the size obtained from HRSEM. The EDX mapping images of the $SnFe_2O_4$ (ST) nanoparticles also clearly reveal that Fe, O, and Sn elements are all distributed uniformly throughout the sample. High-resolution transmission electron microscopy (HRTEM, Fig. 2d) indicates that the *d*-spacing is 2.965 Å. This value is very close to that of Fe_3O_4 (220) planes (2.966 Å). The inset of Fig. 2d shows the fast Fourier transform (FFT) from the shown image, which demonstrates the good crystallinity of the $SnFe_2O_4$ (ST) nanoparticles.

3.2 Magnetic properties

Fig. 3a shows the magnetic hysteresis loops for the $SnFe_2O_4$ (ST) and $SnFe_2O_4$ (PE) nanoparticles at 298 K. The saturation magnetization value M_s and the coercivity value H_c of the $SnFe_2O_4$ (ST) nanoparticles are as high as 74.3 emu g^{-1} and 110 Oe, whereas the M_s value of $SnFe_2O_4$ (PE) nanoparticles is only 5 emu g^{-1}. Fig. 3b shows the previously reported M_s values of $SnFe_2O_4$ synthesized by various aqueous methods, indicating that the $SnFe_2O_4$ (ST) nanoparticles prepared in this work have a much higher M_s value than those reported for other $SnFe_2O_4$ nanoparticles. Since it is widely acknowledged that the decrease in the ferrite nanoparticles size can result in reduced M_s due to the magnetically dead layer on the surface of the particles,[14,33]

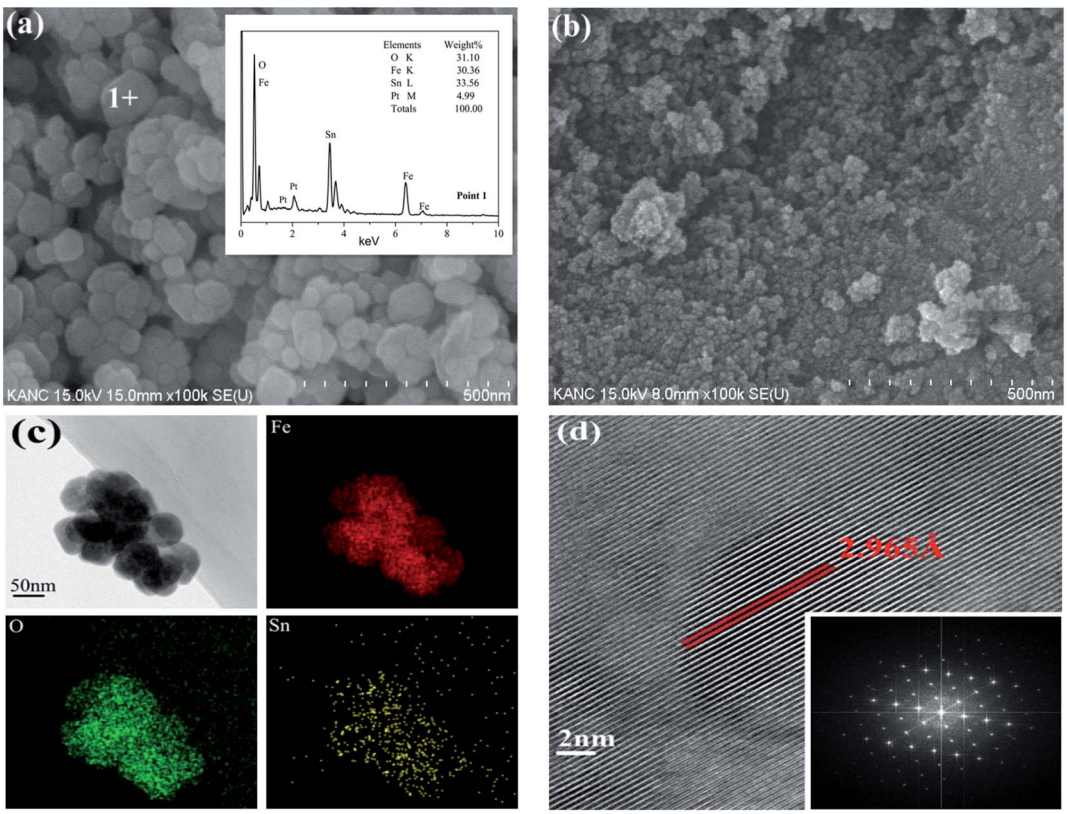

Fig. 2 (a) HRSEM of $SnFe_2O_4$ (ST) and (b) HRSEM of $SnFe_2O_4$ (PE) nanoparticles. The inset in (a) shows the EDX analysis of point 1, (c) TEM and EDX elemental mapping images for $SnFe_2O_4$ (ST) nanoparticles, (d) HRTEM image showing the lattices of $SnFe_2O_4$ (ST) nanoparticles, the inset is the FFT pattern observed from the corresponding image.

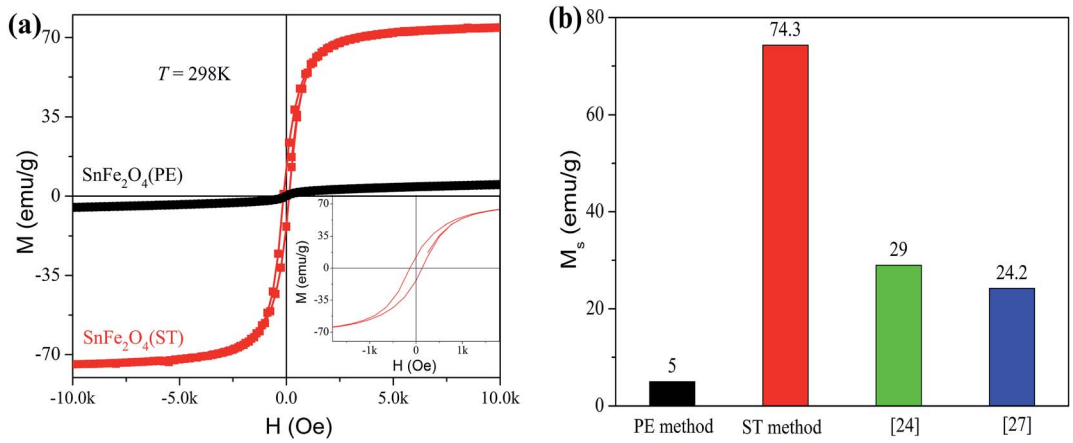

Fig. 3 (a) M–H loops recorded at 298 K from $SnFe_2O_4$ nanoparticles synthesized by different method, and the inset is an enlarged hysteresis loops at low H field. (b) Comparison of M_s of $SnFe_2O_4$ nanoparticles in this work and previous reports.

the relatively larger particle size of $SnFe_2O_4$ (ST) can attribute to the observed high magnetization considering that most of the reported sizes of $SnFe_2O_4$ nanoparticles were less than 10 nm.[27,30] In addition, Chen *et al.*[34] reported that improved the magnetic property of ferrite nanoparticles can be ascribed to the introduction of Fe^{2+} as a precursor, which led to the redistribution of cations in the tetrahedral-sites and the octahedral-sites in the spinel lattices.

3.3 FT-IR, PL and UV-vis DRS spectra

The FT-IR spectra of $SnFe_2O_4$ nanoparticles prepared by ST method are presented in Fig. 4a. The bands at 3439.21 cm^{-1} and 1636.15 cm^{-1} may be assigned to hydroxyls,[35] and the two characteristic peaks are observed at 563.81 cm^{-1} and 446.77 cm^{-1} can be attributed to the vibrations of Sn–O and Fe–O bonds, respectively.[27] Therefore, the FT-IR spectrum result further confirms the composition of $SnFe_2O_4$. The optical property of the as-prepared materials was studied by the UV-vis DRS and PL analyses, and the results are shown in Fig. 4b. The inset of Fig. 4b shows the UV-vis DRS spectra of the pure TiO_2 (anatase TiO_2, 99.8% purity, particle size of 60 nm, Aladdin Chemistry Co., Ltd, Shanghai, China) and $SnFe_2O_4$ (ST) nanoparticles. Pure TiO_2 only absorbed the ultraviolet radiation with wave length of less than 400 nm, whereas the $SnFe_2O_4$ (ST) nanoparticles exhibited a much enhanced absorbance in the visible light region of 400–800 nm, implying the possibility of making the most of solar light. The enhanced light absorption can produce more photogenerated electron–hole (e^-–h^+) pairs, and resulting in a higher photocatalytic activity. The PL analysis is a well-known as a method to evaluate the separation efficiency of the photogenerated e^-–h^+ pairs in a photocatalyst. The PL spectra of the pure TiO_2 and $SnFe_2O_4$ (ST) nanoparticles with an excitation wavelength of 420 nm are depicted in Fig. 4b, and the much weaker PL signals from the $SnFe_2O_4$ (ST) nanoparticles indicates a lower recombination rate of the e^-–h^+ pairs. Thus the $SnFe_2O_4$ (ST) nanoparticles may be served as a favorable pathway for the transfer of the photogenerated charge carriers.

3.4 XPS surface analysis

In order to determine the surface chemical composition and the valence state of the $SnFe_2O_4$ (ST) nanoparticles, XPS spectra were collected in Fig. 5 and the C 1s, O 1s, Fe 2p and Ti 2p peaks were observed. The C 1s peak was assigned to the adventitious

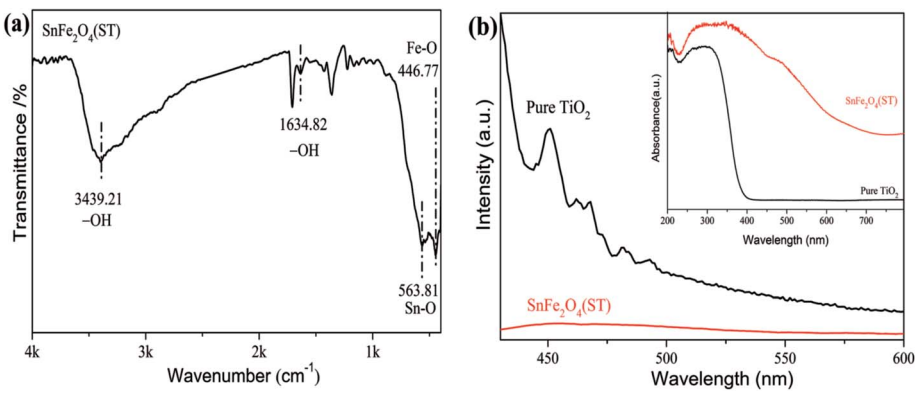

Fig. 4 (a) FT-IR spectrum of $SnFe_2O_4$ (ST) nanoparticles, (b) PL and UV-vis DRS (inset b) spectra of pure TiO_2 and $SnFe_2O_4$ (ST) nanoparticles.

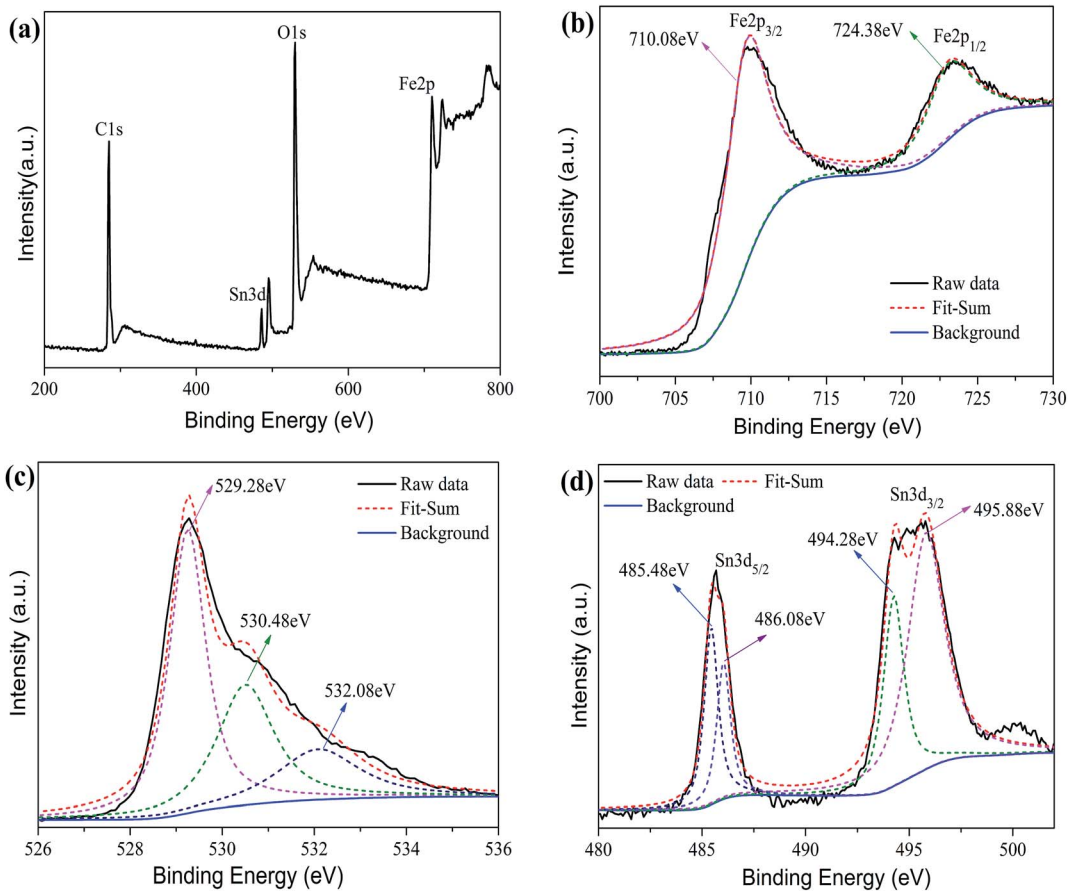

Fig. 5 XPS spectra of $SnFe_2O_4$ (ST) nanoparticles, (a) is a typical XPS wide survey, (b), (c) and (d) are typical high resolution XPS spectra in the Fe 2p, O 1s and Sn 3d region of $SnFe_2O_4$ (ST) nanoparticles.

carbon, and the O 1s, Fe 2p and Sn 3d peaks were ascribed to the $SnFe_2O_4$ (ST) nanoparticles. Fig. 5b–d displays the detailed XPS spectra of Fe, O and Sn, respectively. The peak located at 710.08 eV and 724.38 eV was attributed to the spin–orbit splitting of the Fe $2p_{3/2}$ and Fe $2p_{1/2}$, respectively, which can be ascribed to Fe(III) oxide.[21] No other Fe-related peak was observed in the XPS analysis, suggesting that only Fe(III) exists in the synthetic $SnFe_2O_4$. The peaks at 529.28 eV, 530.48 eV and 532.08 eV in the O 1s are generally ascribed to the chemisorbed oxygen at grain boundaries, on the surface of sample, and the lattice oxygen and hydroxyl O atoms.[36,37] The two peaks at 485.48 eV and 494.28 eV in the XPS spectrum of Sn can be assigned to Sn(II).[38] The other two peaks at 495.88 eV and 486.08 eV are from the lattice tin (Sn(IV) oxidation state), implying that some Sn(II) was oxidized to Sn(IV).[39,40] Therefore, the XPS results confirm that both Sn(II) and Sn(IV) ions are coexisting in $SnFe_2O_4$ (ST) nanoparticles.

3.5 Photocatalytic performance of $SnFe_2O_4$ nanoparticles

In this section, the photocatalytic performances of $SnFe_2O_4$ were evaluated by degradation of CTC, which chemical structure was shown in the inset of Fig. 6a. The changes in the UV-vis spectra from the CTC solution as a function of reaction time under visible light irradiation in the presence of $SnFe_2O_4$ (ST)/9 mM H_2O_2 were shown in Fig. 6a. The absorption peak at 354 nm drops gradually with increasing irradiation time (visible light irradiation time from 0 min to 150 min), indicating that the $SnFe_2O_4$ (ST)/9 mM H_2O_2 exhibits an excellent photocatalytic activity during the reaction. Fig. 6b shows the evolution of the visible light irradiation time (t) dependence of the ratio between the normalized CTC concentration (C_t) and its initial concentration (C_0) when different catalysts were used. The following two conclusions can be drawn from this figure: firstly, the presence of H_2O_2 greatly improved the photocatalytic efficiency, and secondly, the degradation of CTC is much faster with $SnFe_2O_4$ (ST) than $SnFe_2O_4$ (PE) and TiO_2. Therefore the overall efficiency of CTC followed an order of $SnFe_2O_4$ (ST)/9 mM H_2O_2 > $SnFe_2O_4$ (PE)/9 mM H_2O_2 > TiO_2/9 mM H_2O_2 > $SnFe_2O_4$ (ST) > $SnFe_2O_4$ (PE) > TiO_2. The lower decay rate of the CTC concentration when only TiO_2 was used is mainly due to the wide bandgap energy of TiO_2 as 3.2 eV, so that it is inactive under visible light.[32] Between the two $SnFe_2O_4$ samples, the worse performance observed from $SnFe_2O_4$ (PE) than $SnFe_2O_4$ (ST) can be attributed to the higher amount of defects in $SnFe_2O_4$ (PE) acting as e^-–h^+ recombination centers.[41,42]

The chemical catalyzation process of CTC by $SnFe_2O_4$ (ST)/9 mM H_2O_2 can be briefly explained using the following equations. Firstly, the CTC molecules were adsorbed onto the

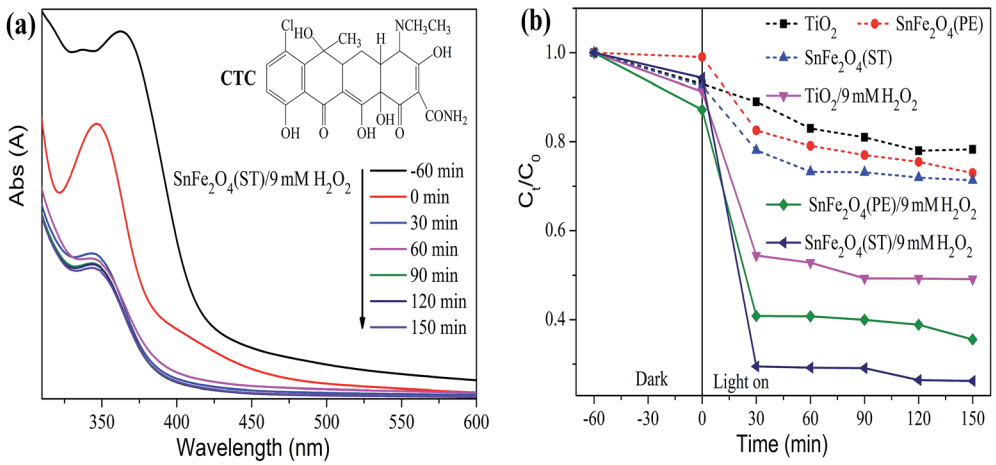

Fig. 6 (a) Time-dependent optical absorbance spectra of CTC ($C_0 = 50$ mg L^{-1}) solution in the presence of $SnFe_2O_4$ (ST)/9 mM H_2O_2 after exposure to visible light, the inset figure shows the chemical structures of CTC, (b) C_t/C_0 *versus* time curves for CTC ($C_0 = 50$ mg L^{-1}) solution containing $SnFe_2O_4$ (ST), $SnFe_2O_4$ (PE), TiO_2, $SnFe_2O_4$ (ST)/9 Mm H_2O_2, $SnFe_2O_4$ (PE)/9 mM H_2O_2 and TiO_2/9 mM H_2O_2.

surface of $SnFe_2O_4$ (eqn (1)). The e^- and h^+ pairs are generated when the $SnFe_2O_4$ suspension is irradiated with the visible light (eqn (2)). Part of photogenerated h^+ and e^- can diffuse to the surface of the catalyst particles and react with the absorbed H_2O and O_2 to create reactive oxygen species (ROS), such as $HO^{\bullet}$ and $O_2^{-\bullet}$ (eqn (3) and (4)).[43] These ROS directly participate in the degradation of CTC. Additionally, H_2O_2 can react with Fe^{3+} in $SnFe_2O_4$ to produce $HO_2^{\bullet}$ and reduce Fe^{3+} to Fe^{2+}

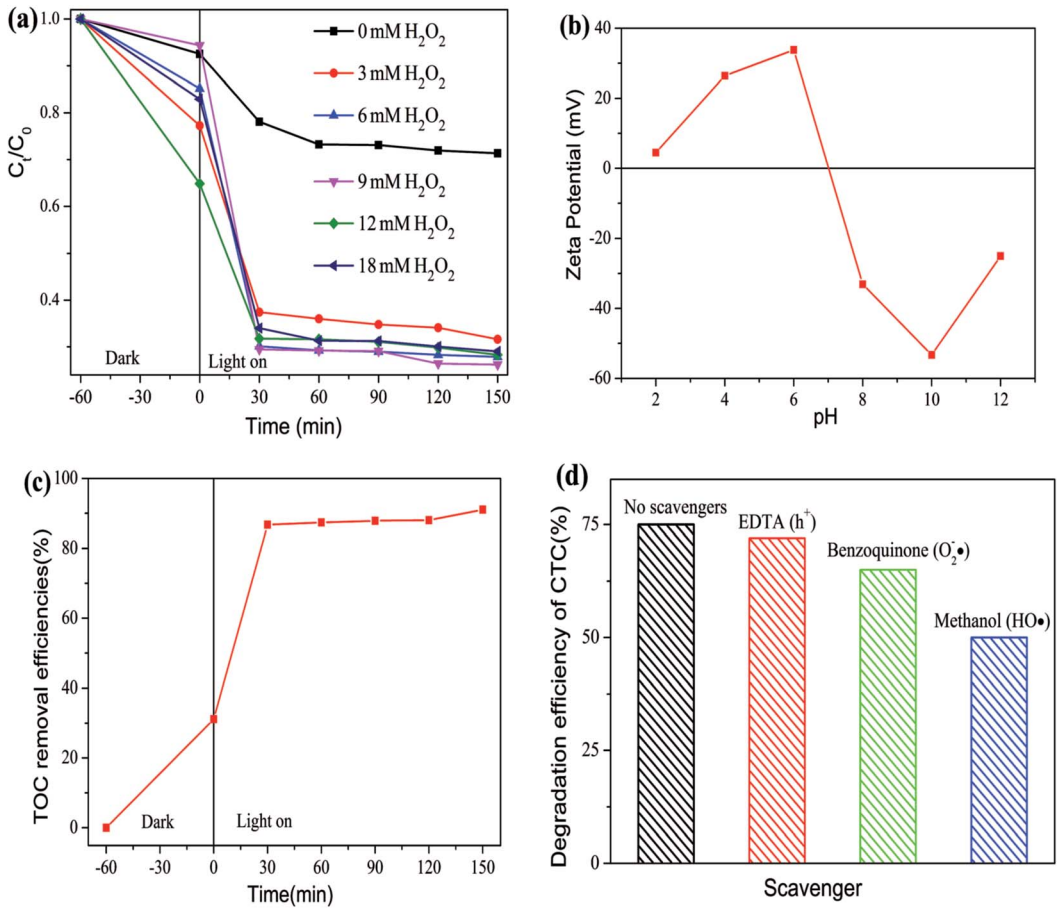

Fig. 7 (a) Photocatalytic degradation of CTC ($C_0 = 50$ mg L^{-1}) using the $SnFe_2O_4$ (ST) with different H_2O_2 concentrations under the visible light, and (b) the zeta-potential of the aqueous dispersions of $SnFe_2O_4$ (ST) at different pH values. (c) The changes of TOC in the presence of $SnFe_2O_4$ (ST)/9 mM H_2O_2 after exposure to visible light. (d) Effects of series of scavengers on the degradation efficiency of CTC.

(eqn (5)).[30,44] Simultaneously, H_2O_2 can also oxidize the continuously regenerated Fe^{2+} (eqn (6)) to create $HO^{\bullet}$ and regenerate Fe^{3+}.[21,45] Therefore, more $HO_2^{\bullet}$ and $HO^{\bullet}$ could be generated for the photocatalytic degradation of CTC. Most of e^- were more likely to be captured by H_2O_2 that apparently prevent the recombination of the e^-–h^+ pairs (eqn (7)),[46] and produce $HO^{\bullet}$ that improves the photocatalytic activities. As very strong oxidizing agents, the $O_2^{-\bullet}$, $HO_2^{\bullet}$, $HO^{\bullet}$ and h^+ radicals can oxidize most of TC antibiotics to the mineral end-products (eqn (8)).[47]

$$SnFe_2O_4 + CTC \xrightarrow{\text{adsorption}} (SnFe_2O_4) - CTC \quad (1)$$

$$SnFe_2O_4 + h\nu \rightarrow SnFe_2O_4\,(e^- + h^+) \quad (2)$$

$$h^+ + H_2O \rightarrow HO^{\bullet} + H^+ \quad (3)$$

$$e^- + O_2 \rightarrow O_2^{-\bullet} \quad (4)$$

$$Fe^{3+} + H_2O_2 \rightarrow Fe^{3+} + HO_2^{\bullet} + H^+ \quad (5)$$

$$Fe^{2+} + H_2O_2 \rightarrow Fe^{3+} + HO^{\bullet} + H^+ \quad (6)$$

$$e^- + H_2O_2 \rightarrow HO^{\bullet} + OH^- \quad (7)$$

$$CTC + HO_2^{\bullet}/HO^{\bullet}/h^+/O_2^{-\bullet} \rightarrow \text{degraded products} \quad (8)$$

Since the presence of H_2O_2 was shown to dramatically improve the degradation rate of CTC, the initial H_2O_2 concentration should be a very important variable. Fig. 7a shows the dependence of the photocatalytic activity of $SnFe_2O_4$ (ST) on the initial H_2O_2 concentration in the range of 0 to 18 mM. The photocatalytic activity of $SnFe_2O_4$ (ST) was found firstly increased quickly when the initial concentration of H_2O_2 increases from 0 to 9 mM, which is mostly due to the generation of more $HO_2^{\bullet}$ and $HO^{\bullet}$ radicals when more H_2O_2 was added into reaction system. The photocatalytic degradation efficiency reached the highest value for $SnFe_2O_4$ (ST)/9 mM H_2O_2, then decreased even though the initial concentration H_2O_2 increased. It has been reported that extra H_2O_2 can also act as a $HO^{\bullet}$ radical scavenger through the formation of $HO_2^{\bullet}$ radicals, which would consequently react with $HO^{\bullet}$ ($HO^{\bullet} + H_2O_2 \rightarrow HO_2^{-\bullet} + OH^-$ and $HO_2^{-\bullet} + HO^{\bullet} \rightarrow O_2 + H_2O$), thus consume the $HO^{\bullet}$ and $HO_2^{\bullet}$ radicals that should have degraded CTC.[21,48] Additionally, the initial concentration of H_2O_2 can affect the absorption of CTC on the photocatalyst surface through the change of pH value in the reaction solution. Fig. 7b gives the pH-dependent zeta potential of $SnFe_2O_4$ (ST), indicating that the point of zero charges (pH_{PZC}) of $SnFe_2O_4$ (ST) is about 7. In our experiment, the initial pH value of the CTC solution is around 7.4, and the pH value of the CTC solution decreased with the addition of H_2O_2. Therefore, the surface of the $SnFe_2O_4$ (ST) particles is positively charged. When the pH value of the CTC solution is in the range of 3.5 < pH <

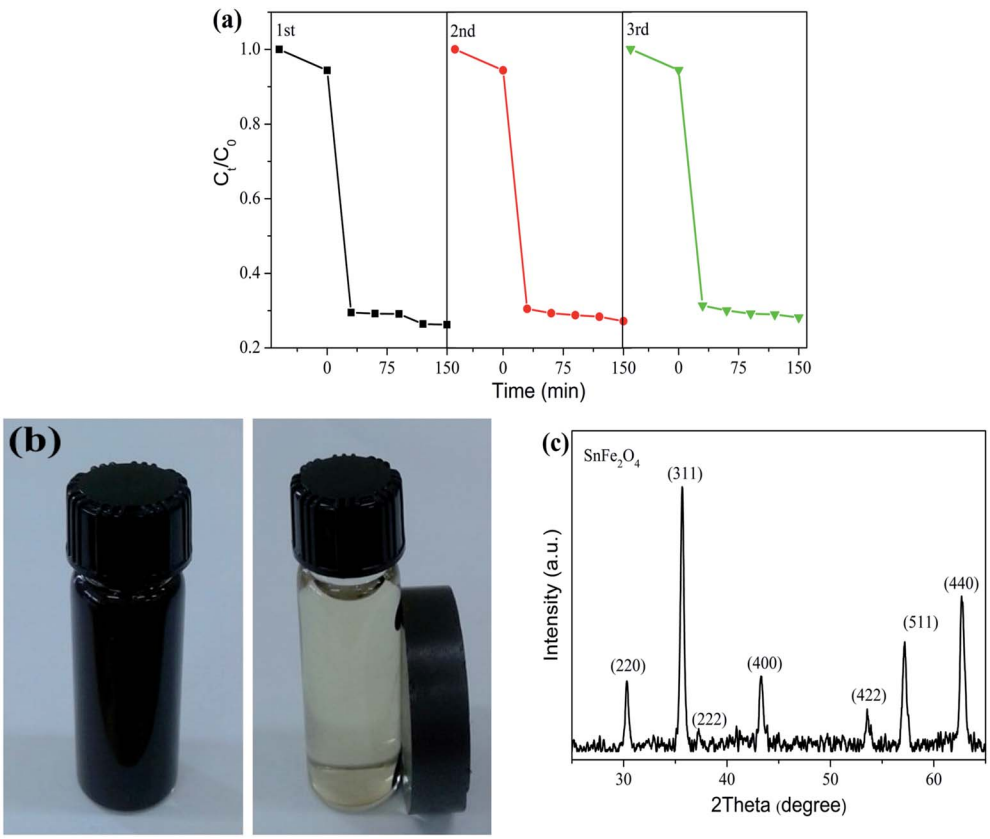

Fig. 8 (a) Three cycle runs of $SnFe_2O_4$ (ST)/9 Mm H_2O_2 for CTC ($C_0 = 50$ mg L^{-1}) degradation under the visible light irradiation, (b) the magnetic separation process of $SnFe_2O_4$ (ST) from a CTC solution and (c) XRD patterns of $SnFe_2O_4$ (ST) after three reaction cycles.

pH_{PZC}, the majority of CTC exists as $CTCH^{2\pm}$,[11] and these radicals may have a relatively stronger adsorption on the surface of $SnFe_2O_4$ (ST) and significantly promote the degradation of CTC. However, when the pH value decreased further to less than 3.5 with the increase of the initial H_2O_2 concentration, CTC is believed to be protonated as $CTCH^{3+}$.[11] In this case, it will be difficult for CTC to be absorbed on the positive charged surface of $SnFe_2O_4$ (ST) because of the electrostatic interaction, which results in the decrease of the CTC degradation rate. Therefore, the initial H_2O_2 concentration may affect the photocatalytic degradation efficiency of CTC through its influence in both photocatalytic reaction and adsorption process, although detailed photocatalytic mechanism and dynamics of $SnFe_2O_4/H_2O_2$ under visible light condition should be further studied in future works.

The TOC degradation depicted in Fig. 7c clearly evidences that the TOC removal efficiencies of CTC within 150 min was 60% over $SnFe_2O_4/H_2O_2$ under visible light condition. Only 31% TOC was removed by adsorption. The results demonstrated that most CTC can be eliminated by the $SnFe_2O_4/H_2O_2$/visible light process. To investigate the photocatalytic mechanism of $SnFe_2O_4/H_2O_2$, a radical trapping experiment was performed to explore the reactive radical species involved in the CTC degradation over $SnFe_2O_4/H_2O_2$. EDTA (10 mM), benzoquinone (10 mM), and methanol (1 : 20/v/v) were added into the reaction system for trapping the specific reactive species h^+, $O_2^{-\bullet}$ and $HO^\bullet$, respectively. As shown in Fig. 7d, under visible light, the photocatalytic degradation of CTC was hardly inhibited after adding the h^+ scavenger (EDTA), which revealed that h^+ contributed to a lesser extent in CTC degradation. Then, as the $O_2^{-\bullet}$ and $HO^\bullet$ scavenger (methanol and benzoquinone) were added, the photocatalytic degradation efficiencies of CTC also decreased to 65% and 50%, respectively. It was illustrated that the $O_2^{-\bullet}$ and $HO^\bullet$ were the major active species in this system under visible light irradiation.

3.6 Durability of $SnFe_2O_4$ nanoparticles

Fig. 8a shows the stability and the reusability of the $SnFe_2O_4$ (ST) photocatalyst in three continuous runs under the visible light illumination. Obviously even after three cycles the efficiency of $SnFe_2O_4$ (ST) for the photocatalytic degradation of CTC were maintained above 70% at 150 min and barely declined, indicating an adequate stability in the CTC pollutants elimination. The $SnFe_2O_4$ (ST) nanoparticles are easily dispersed in the CTC solution to form a darker viscous fluid. The high superparamagnetism of $SnFe_2O_4$ (ST) ensures the photocatalyst nanoparticles to be easily separated from their aqueous dispersions within 5 s using an external magnet (Fig. 8b), and the suspension became transparent immediately. The excellent reusability and easy retrieval promise the $SnFe_2O_4$ (ST) nanoparticles for the removal of the residual CTCs in the wastewater system. The diffraction patterns (Fig. 8c) of $SnFe_2O_4$ (ST) catalyst after 3 cycles (used catalyst) of testing of photocatalytic activity were essentially similar to that of $SnFe_2O_4$ before the photocatalytic testing, and no noticeable deviation was observed, indicative of high stability of $SnFe_2O_4$ (ST) samples.

4. Conclusions

We successfully prepared inverse spinel $SnFe_2O_4$ nanoparticles through a simple, cost-effective, and low temperature solvothermal method. As compared to the $SnFe_2O_4$ nanoparticles prepared through other approached, much improved crystallinity and much higher saturation magnetization was observed from the solvothermally synthesized $SnFe_2O_4$ nanoparticles. These properties paved the way for the excellent photocatalytic degradation of CTC using $SnFe_2O_4/H_2O_2$ under the illumination of visible light. The detailed investigation of the photocatalyst process revealed that the optimum performance can be obtained with an initial concentration of H_2O_2 as 9 mM. We also demonstrated that the $SnFe_2O_4$ nanoparticles can be fast collected magnetically and used repeatedly after recycle. Our results show that $SnFe_2O_4$ nanoparticles can be a promising catalyst for the removal of residual CTC from the water system.

Acknowledgements

This research was supported by the Basic Science Research Program through the National Research Foundation of Korea funded by the Ministry of Science, ICT and Future Planning (2014R1A1A3049826 and 2014R1A2A1A11051245). SEM characterization in this research was supported by Nano-material Technology Development Program through the National Research Foundation of Korea (NRF) funded by the Ministry of Science, ICT and Future Planning (2009-0082580). The XPS measurement was performed in Busan Center of Korea Basic Science Institute (KBSI). The authors would like to thank Advanced Functional Material Lab of Shanghai University for the experimental assistance on the UV-vis DRS measurements.

References

1 A. K. Sarmah, M. T. Meyer and A. B. Boxall, *Chemosphere*, 2006, **65**, 725–759.
2 R. X. Guo and J. Q. Chen, *Chemosphere*, 2012, **87**, 1254–1259.
3 R. Daghrir, P. Drogui and M. A. El Khakani, *Electrochim. Acta*, 2013, **87**, 18–31.
4 R. Andreozzi, M. Raffaele and P. Nicklas, *Chemosphere*, 2003, **50**, 1319–1330.
5 T. Heberer, *J. Hydrol.*, 2002, **266**, 175–189.
6 R. Daghrir, P. Drogui, N. Delegan and M. A. El Khakani, *Water Res.*, 2013, **47**, 6801–6810.
7 R. Daghrir, P. Drogui, N. Delegan and M. A. El Khakani, *Sci. Total Environ.*, 2014, **466**, 300–305.
8 T. H. Kim, S. D. Kim, H. Y. Kim, S. J. Lim, M. Lee and S. Yu, *J. Hazard. Mater.*, 2012, **227**, 237–242.
9 G. Chen, L. Zhao and Y. H. Dong, *J. Hazard. Mater.*, 2011, **193**, 128–138.
10 Y. Chen, H. Li, Z. Wang, T. Tao, D. Wei and C. Hu, *J. Environ. Sci.*, 2012, **24**, 254–260.
11 J. J. Salazar-Rábago, M. Sánchez-Polo, J. Rivera-Utrilla, R. Leyva-Ramos and R. Ocampo-Pérez, *Chem. Eng. J.*, 2016, **284**, 896–904.
12 D. Bu and H. Zhuang, *Appl. Surf. Sci.*, 2013, **265**, 677–685.

13 Y. Liu, L. Yu, Y. Hu, C. Guo, F. Zhang and X. W. D. Lou, *Nanoscale*, 2012, **4**, 183–187.
14 M. P. Reddy and A. M. A. Mohamed, *Microporous Mesoporous Mater.*, 2015, **215**, 37–45.
15 Y. Liu, L. Zhou, Y. Hu, C. Guo, H. Qian, F. Zhang and X. W. D. Lou, *J. Mater. Chem.*, 2011, **21**, 18359–18364.
16 Y. Wang, J. Ning, E. Hu, C. Zheng, Y. Zhong and Y. Hu, *J. Alloys Compd.*, 2015, **637**, 301–307.
17 Z. Zhu, X. Li, Q. Zhao, Y. Shi, H. Li and G. Chen, *J. Nanopart. Res.*, 2011, **13**, 2147–2155.
18 L. Han, X. Zhou, L. Wan, Y. Deng and S. Zhan, *J. Environ. Chem. Eng.*, 2014, **2**, 123–130.
19 Y. Shen, L. Wang, Y. Wu, X. Li, Q. Zhao, Y. Hou and W. Teng, *Catal. Commun.*, 2015, **68**, 11–14.
20 P. Xiong, Y. Fu, L. Wang and X. Wang, *Chem. Eng. J.*, 2012, **195**, 149–157.
21 C. Cai, Z. Zhang, J. Liu, N. Shan, H. Zhang and D. D. Dionysiou, *Appl. Catal., B*, 2016, **182**, 456–468.
22 A. A. Al-Kahtani and M. F. A. Taleb, *J. Hazard. Mater.*, 2016, **309**, 10–19.
23 Y. Zhou, B. Xiao, S. Q. Liu, Z. Meng, Z. G. Chen, C. Y. Zou and X. Zhou, *Chem. Eng. J.*, 2016, **283**, 266–275.
24 S. Q. Liu, B. Xiao, L. R. Feng, S. S. Zhou, Z. G. Chen, C. B. Liu and Z. D. Meng, *Carbon*, 2013, **64**, 197–206.
25 F. Liu, T. Li and H. Zheng, *Phys. Lett. A*, 2004, **323**, 305–309.
26 F. X. Liu and T. Z. Li, *Mater. Lett.*, 2005, **59**, 194–196.
27 H. Elmoussaoui, M. Hamedoun, O. Mounkachi, A. Benyoussef, R. Masrour and E. K. Hlil, *J. Supercond. Novel Magn.*, 2012, **25**, 1995–2002.
28 K. El Maalam, M. B. Ali, H. El Moussaoui, O. Mounkachi, M. Hamedoun, R. Masrour and A. Benyoussef, *J. Alloys Compd.*, 2015, **622**, 761–764.
29 O. N. C. Uwakweh, R. Más, C. Morales, P. Vargas, J. Silva, A. Rosa and Y. Cardona, *J. Mater. Eng. Perform.*, 2011, **20**, 1157–1162.
30 K. T. Lee and S. Y. Lu, *J. Mater. Chem. A*, 2015, **3**, 12259–12267.
31 P. Rai, R. K. Gautam, S. Banerjee, V. Rawat and M. C. Chattopadhyaya, *J. Environ. Chem. Eng.*, 2015, **3**, 2281–2291.
32 H. Liu, K. Shon, X. Sun, S. Vigneswaran and H. Nan, *Appl. Surf. Sci.*, 2011, **257**, 5813–5819.
33 D. Cao, X. Wang, L. Pan, H. Li, P. Jing, J. Wang and Q. Liu, *J. Mater. Chem. C*, 2016, **4**, 951–957.
34 Z. P. Chen, W. Q. Fang, B. Zhang and H. G. Yang, *J. Alloys Compd.*, 2013, **550**, 348–352.
35 R. Li, Y. Jia, J. Wu and Q. Zhen, *RSC Adv.*, 2015, **5**, 40764–40771.
36 X. Zhu, F. Zhang, M. Wang, J. Ding, S. Sun, J. Bao and C. Gao, *Appl. Surf. Sci.*, 2014, **319**, 83–89.
37 R. Al-Gaashani, S. Radiman, N. Tabet and A. R. Daud, *Mater. Sci. Eng., B*, 2012, **177**, 462–470.
38 X. Tian, Z. Pan, H. Zhang, H. Fan, X. Zeng, C. Xiao and Z. Wei, *Ceram. Int.*, 2013, **39**, 6497–6502.
39 G. H. Zhang, P. Y. Wang, X. Y. Deng, Y. Chen, D. J. Gengzang, X. L. Wang and W. J. Chen, *Mater. Lett.*, 2016, **162**, 265–268.
40 F. D. O. Cantão, W. D. C. Melo, L. C. A. Oliveira, A. R. Passos and A. C. D. Silva, *Quim. Nova*, 2010, **33**, 528–531.
41 B. V. Kumar, M. D. Prasad and M. Vithal, *Mater. Lett.*, 2015, **152**, 200–202.
42 C. Zhang and Y. Zhu, *Chem. Mater.*, 2005, **17**, 3537–3545.
43 L. Han, X. Zhou, L. Wan, Y. Deng and S. Zhan, *J. Environ. Chem. Eng.*, 2014, **2**, 123–130.
44 B. Palanisamy, C. M. Babu, B. Sundaravel, S. Anandan and V. Murugesan, *J. Hazard. Mater.*, 2013, 233–242.
45 K. T. Lee and S. Y. Lu, *J. Mater. Chem. A*, 2015, **3**, 18578–18585.
46 Y. Yao, J. Qin, H. Chen, F. Wei, X. Liu, J. Wang and S. Wang, *J. Hazard. Mater.*, 2015, **291**, 28–37.
47 Z. Zhu, Z. Lu, D. Wang, X. Tang, Y. Yan, W. Shi and H. Dong, *Appl. Catal., B*, 2016, **182**, 115–122.
48 M. Su, C. He, V. K. Sharma, M. A. Asi, D. Xia, X. Z. Li and Y. Xiong, *J. Hazard. Mater.*, 2012, **211**, 95–103.